

Cite this: *J. Mater. Chem. C*, 2025, 13, 23083

Thermoelectric properties of topological Weyl semimetal family RAIX (R = La, Ce, Nd; X = Si, Ge): a first-principles investigation

Soumyojit Chatterjee,^{ID} Pratyasha Tripathy,^{ID} Karthik Arya Pradhan and Rahul Sharma^{ID}*

Weyl semimetals have emerged as an exciting class of materials with a myriad of non-trivial transport properties due to their topological nature. In this work, we investigate the thermoelectric properties of various experimentally reported members of a Weyl semimetal family RAIX for R = La, Ce and Nd and X = Si and Ge using first-principles calculations within the semi-classical Boltzmann transport theory. Our comprehensive analysis of the electronic structure and phonon dispersion sheds light on various aspects of thermoelectric transport in this family of materials. Our calculations show that the transport in RAIX is dominated by the d-orbitals of R and the p-orbitals of Al and X. We also discover that the phonon contribution to the thermal conductivity is much smaller compared to the electronic contribution, a desirable factor for thermoelectrics. We report the highest value of thermoelectric figure of merit $zT = 0.56$ for CeAlGe at 900 K, which is encouraging when compared among semimetals. Our work reveals that the combination of topologically non-trivial Weyl dispersion and the presence of heavy elements in the RAIX family offers a promising avenue for thermoelectric applications in Weyl semimetals and therefore makes multifunctional applications possible.

Received 19th June 2025,
Accepted 6th October 2025

DOI: 10.1039/d5tc02363g

rsc.li/materials-c

1. Introduction

The energy requirements have been ever increasing and they are now accelerated by the big data and server requirements of artificial intelligence (AI), which is becoming an integral part of global technology rapidly. There is an urgent need to look for alternative forms of energy. Most of the industrial processes, including the servers, produce a lot of heat. Thermoelectric materials are able to convert heat into electricity.^{1–3} Thermoelectric devices do not require any moving parts, making them very useful for a multitude of applications, including space deployments,⁴ integration into microprocessors for cooling,⁴ and wearable electronics to convert body heat into electricity to charge small electronic devices.^{5–7} Therefore, thermoelectric materials offer a promising route towards a sustainable future as the current technology trends demand.⁴

The performance of a thermoelectric material is characterized by a thermoelectric figure of merit,^{3,8,9} defined as

$$zT = \frac{S^2 \sigma T}{\kappa} \quad (1)$$

Indian Institute of Science Education and Research Berhampur, Berhampur 760003, Odisha, India. E-mail: rahulsharma@iiserbpr.ac.in

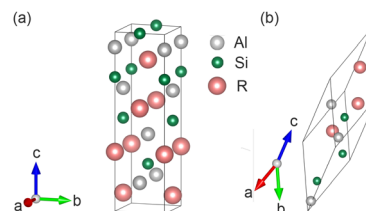


Fig. 1 (a) The conventional body-centered tetragonal unit cell of RAIX showing different layers of atoms. Each layer contains only one type of atom. (b) The primitive unit cell used for our calculations.

Table 1 Lattice constants obtained using DFT after relaxation of the lattice and corresponding experimental lattice constants of LaAlSi,⁷² LaAlGe,⁷² CeAlSi,⁷³ CeAlGe,⁷⁴ NdAlSi,⁷³ and NdAlGe⁴⁵

| RAIX | Calculated | | Experimental | |
|--------|------------|---------|--------------|---------|
| | a (Å) | c (Å) | a (Å) | c (Å) |
| LaAlSi | 4.3248 | 14.6616 | 4.3130 | 14.6793 |
| LaAlGe | 4.3771 | 14.8666 | 4.3494 | 14.8286 |
| CeAlSi | 4.2842 | 14.6694 | 4.2502 | 14.5769 |
| CeAlGe | 4.3283 | 14.9072 | 4.2920 | 14.7496 |
| NdAlSi | 4.2299 | 14.5463 | 4.2010 | 14.5079 |
| NdAlGe | 4.2824 | 14.7263 | 4.2307 | 14.6364 |



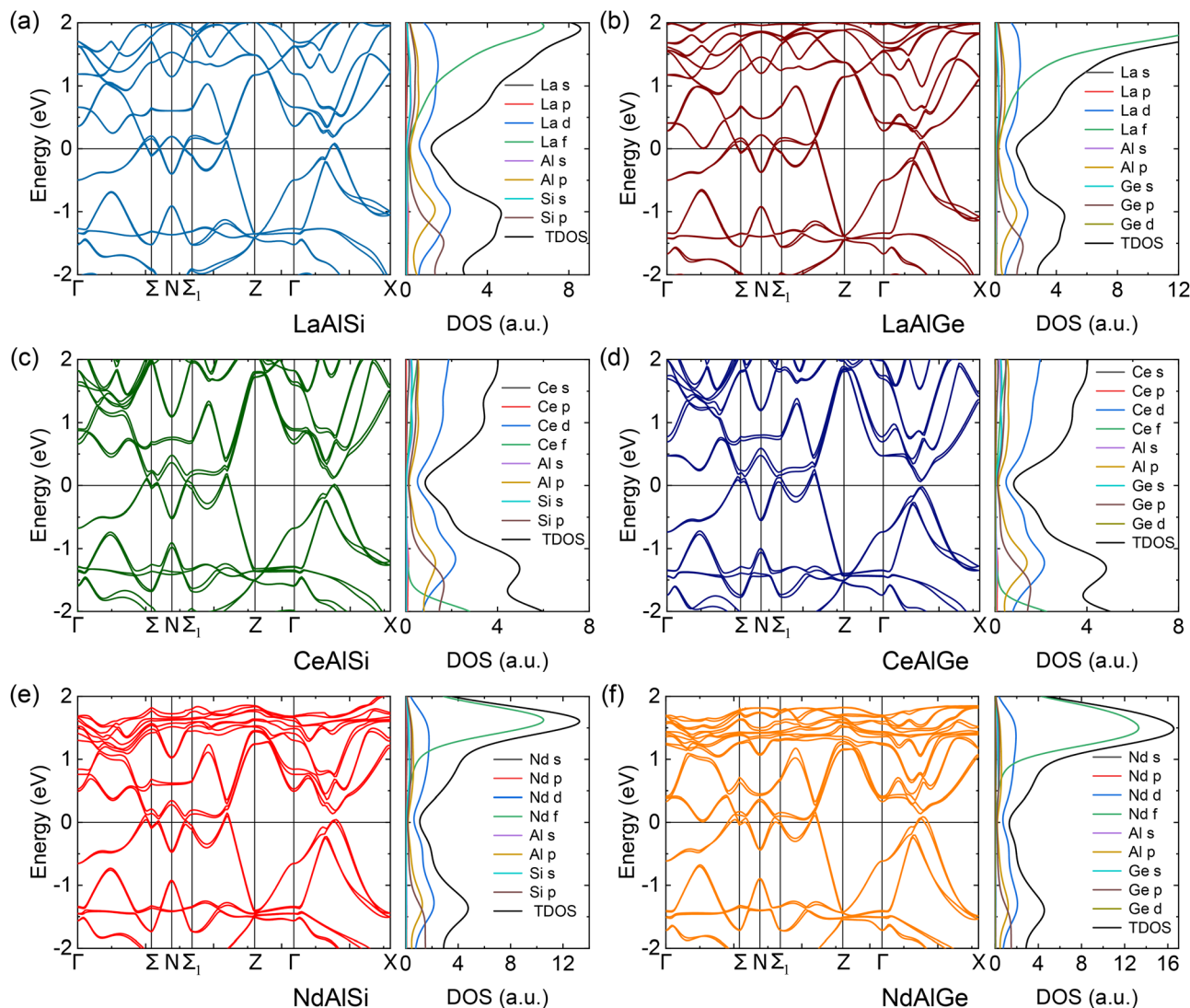


Fig. 2 Electronic band structures of RAIX calculated with Hubbard and SOC interactions, plotted along with the corresponding DOS. The linearly crossing dispersion along Σ -N- Σ_1 indicates Weyl semimetal nature. LaAlX as shown in (a) and (b) have Weyl nodes lying close to the Fermi level while the magnetic nature of Ce and Nd cause the location of the Weyl nodes to shift away as can be seen in (c)–(f). This has implications for carrier polarity and thermoelectric performance. DOS plotted adjacent to the electronic band structures show minima at the Fermi level, characteristic of a semimetal and indicating that the d orbitals of the R and p orbitals of the Al and X are the major players for transport near the Fermi level.

where S is the Seebeck coefficient, which is the electrical potential difference generated per unit thermal gradient, σ is the electrical conductivity, and κ is the thermal conductivity consisting of both electronic and lattice thermal contributions $\kappa = \kappa^{\text{el}} + \kappa^{\text{l}}$. Optimizing this thermoelectric figure of merit is challenging as the parameters involved do not vary in a cooperative fashion.^{9–11} It would be desirable to have poor phonon conductivity and good electron conductivity, a couple of traits that are usually in conflict with each other as κ is proportional to σT due to the Wiedemann–Franz law;¹² thus, increasing the σ increases the κ and nullifies its effect. Increasing σ also decreases S ,¹² and this also makes increasing the zT difficult.

Topological semimetals may offer a way out of this conundrum by providing high mobility Dirac or Weyl dispersion due

Table 2 Maximum zT from our calculations for the RAIX family in both the xx and zz directions and the corresponding μ and T they occur at for each direction

| RAIX | zT_{xx} | zT_{zz} | μ_{xx} | μ_{zz} | T_{xx} | T_{zz} |
|--------|-----------|-----------|------------|------------|----------|----------|
| LaAlSi | 0.29 | 0.30 | 0.14 | 0.20 | 700 | 900 |
| LaAlGe | 0.27 | 0.35 | 0.14 | 0.17 | 700 | 900 |
| CeAlSi | 0.36 | 0.34 | 0.18 | 0.19 | 900 | 900 |
| CeAlGe | 0.39 | 0.56 | 0.17 | 0.19 | 700 | 900 |
| NdAlSi | 0.33 | 0.33 | 0.15 | 0.19 | 700 | 900 |
| NdAlGe | 0.28 | 0.43 | 0.14 | 0.15 | 700 | 700 |

to topology along with the bulk bands, which may provide a high Seebeck coefficient.¹³ The thermoelectric properties of Dirac and Weyl semimetals have garnered recent attention due to their unique band structure and exotic surface states leading



to intriguing transport phenomena like chiral anomaly.^{14–17} In particular, Weyl semimetals have been shown to be a promising platform for a variety of unconventional phenomena in thermal transport such as axial-gravitational anomaly¹⁸ and non-saturating Seebeck coefficient under high magnetic fields.¹⁹ Weyl semimetal TaP shows non-saturating thermopower up to 9 T and giant values up to $525 \mu\text{W cm}^{-1} \text{K}^{-2}$.²⁰ Magnetic Weyl semimetals $\text{Co}_3\text{Sn}_2\text{S}_2$ ²¹ and TbPtBi ²² have been explored experimentally for thermoelectric coefficients. WTe_2 , a flexible Weyl Semimetal, demonstrates ultrahigh Nernst thermopower of $3 \text{ W m}^{-1} \text{K}^{-2}$.²³ Weyl semimetal NbP ²⁴ shows a Nernst thermopower comparable to state-of-the-art thermoelectrics.²⁵ Therefore, Weyl semimetals present a fertile ground to look for possible thermoelectric materials and offer new possibilities based on their topological band structure.

Weyl semimetal family RAlX ($\text{R} = \text{La, Ce, Nd}$; $\text{X} = \text{Si, Ge}$)^{26,27} has been of recent interest with multiple exciting results. LaAlGe has been shown to host tilted Weyl cones using angle-resolved photoemission (ARPES)²⁸ indicating that this material may be a host to Lorentz violating type-II Weyl fermions.²⁹ Type-II Weyl semimetals are an exciting ground for thermoelectric properties as the thermoelectric coefficients are predicted to be strongly enhanced within the semiclassical approach.³⁰ $\text{Co}_3\text{Sn}_2\text{S}_2$, which has shown indications of tilted Weyl cones³¹ has demonstrated a magnetic-field antisymmetric Seebeck effect. Magnetic and magnetotransport experiments have shown signatures of non-trivial topology in CeAlGe ^{32–35} and LaAlSi .³⁶ ARPES experiments have confirmed the Weyl semimetal nature of CeAlSi .²⁷ Optical signatures also indicate towards type-II Weyl fermions in LaAlSi and CeAlSi .³⁷ All these

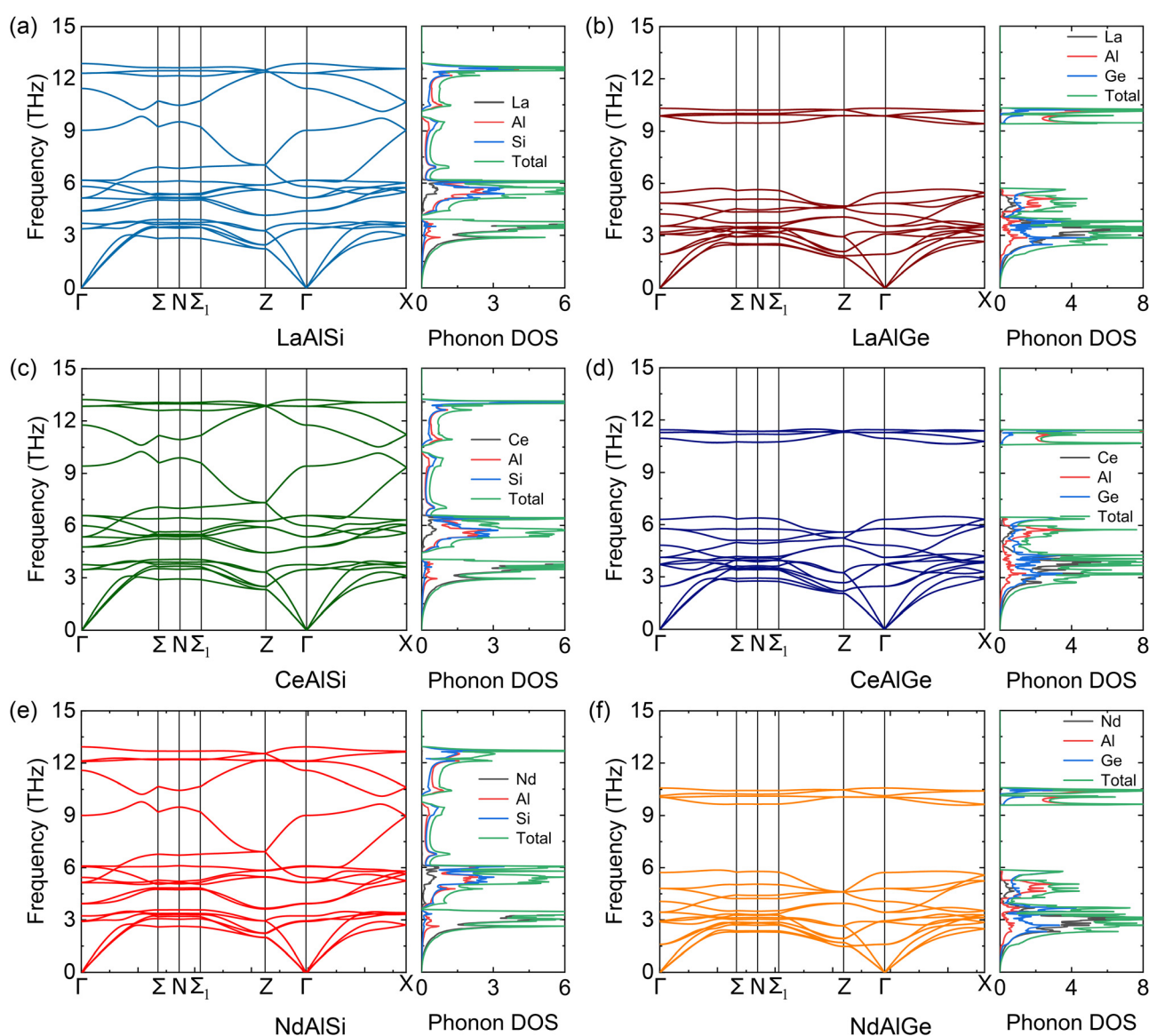


Fig. 3 Phonon dispersions for all the RAlX members considered in this study along with the DOS. There are 3 acoustic modes out of 18 total modes. In RAlGe , the mismatch of masses of Al and Ge leads to a gap in the dispersion in the 6–9 THz frequency region, as can be seen in (b), (d) and (f) as compared to RAlSi in (a), (c) and (e).



aspects make RAlX an attractive platform for investigating functional applications that may benefit from the topological nature. Though electronic transport is well-studied in this family of materials, there is a need to study thermal transport as well. This is important given the wealth of exotic physics Weyl semimetals, especially of the type-II variety, offer.

Motivated thus, in this work, we employ density functional theory (DFT) to investigate the thermoelectric properties of the RAlX family of compounds ($R = \text{La, Ce, Nd}$; $X = \text{Si, Ge}$). We provide a comprehensive analysis of the electronic and the phonon properties of this family of compounds, as both are crucial to determining whether this family of materials can offer potentially better thermoelectrics. The electronic structure reveals the Weyl points, which may aid the thermoelectric figure of merit by their characteristic high mobility. Our phonon-based calculations show significantly low thermal conductivity compared to electronic conductivity. This is a desirable feature as band engineering is not always easy and possible, and the low thermal conductivity route to better thermoelectrics might be favorable. Our semi-classical transport analysis in this family reveals moderate anisotropy in the xx vs. zz direction, indicating which directions might be preferable for devices. Finally, we show the thermoelectric figure of merit zT and compare it with the known topological materials and Weyl semimetals in particular to discuss its implications for the future of thermoelectric devices in this family of materials.

2. Methods

The density functional theory (DFT)^{38,39} calculations presented here are performed with pseudopotentials based on the projector augmented wave (PAW)⁴⁰ method to describe the valence electrons and nuclei interactions as implemented in Quantum Espresso.^{41,42} We have used gradient density approximation to describe the exchange–correlation potential with Perdew–Burke–Ernzerhof (PBE) parametrization.⁴³ Fully relativistic pseudopotentials are employed to include the spin–orbit coupling effects in band structure and density of states (DOS). The self-consistent calculations are performed with an $8 \times 8 \times 8$ Γ -centered k -point mesh chosen as per the Monkhorst–Pack prescription,⁴⁴ with an energy convergence threshold of 2×10^{-7} eV. Our calculations were performed with a high kinetic energy cut-off set to 200 Ry. A Hubbard energy U of 6.0 eV^{45–49} is applied on both Ce and Nd to capture the onsite Coulomb interaction.

Despite exotic charge transport,⁵⁰ the semi-classical formalism has been used to describe the thermoelectric properties⁵¹ effectively. Therefore, we perform our calculations of the electric transport properties under the semi-classical Boltzmann transport theory within the constant relaxation time approximation (CRTA) as implemented in the Boltztrap2 code.^{52,53} This is a widely used method in multiple first-principle studies to calculate transport parameters.^{54–63} A dense $24 \times 24 \times 24$ k mesh is used for non-self-consistent calculations to accurately interpolate the Kohn–Sham eigenvalues. We have used $\tau = 10^{-14}$ s^{55,56,64,65} in our κ^{el} and zT calculations.

We have used PHONOPY for calculating second-order (harmonic) interatomic force constants (IFCs) in the finite displacement method on a $2 \times 2 \times 2$ supercell with a $6 \times 6 \times 6$ k point grid and energy convergence threshold of 1.2×10^{-9} eV to obtain the phonon dispersion relations and phonon DOS. The third-order (anharmonic) IFCs are crucial for considering the phonon–phonon scattering leading to lattice thermal conductivity calculations. We have used PHONO3PY to extract them applied on the same $2 \times 2 \times 2$ supercell^{66,67} and the same energy cutoff. Spin–orbit coupling (SOC) is included in all our phonon calculations. We have also checked the zT values with the calculated relaxation time using density functional perturbation theory (DFPT)⁶⁸ and the electron phonon Wannier (EPW)⁶⁹ package in the SI Fig. S5. To confirm the existence of Weyl points, we have performed the Fermi arc calculations along the (001) surface and chirality calculations using the WANNIER90⁷⁰ and WANNIERTOOLS⁷¹ packages. The results are shown in the SI, Fig. S6 and S7.

3. Results and discussion

3.1 Structural properties

The RAlX family consists of a body-centered tetragonal lattice with the space group $I4_1md$ (no. 109), which lacks inversion symmetry and makes the realization of Weyl semimetals in this family possible. There are 12 layers of atoms along (001), each containing a different type of atomic arrangement in the conventional unit cell as shown in Fig. 1a. We have performed full

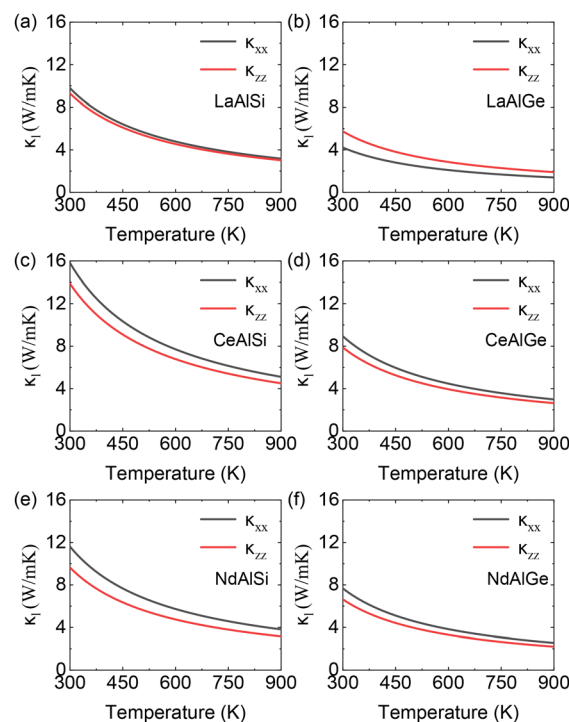


Fig. 4 Lattice thermal conductivities as a function of temperature calculated along the xx and zz directions for all RAlX members in this study. The values of lattice thermal conductivities are low (of the order $10 \text{ W m}^{-1} \text{ K}^{-1}$) compared to the electronic thermal conductivities, as shown in Fig. 8, making them attractive candidates for thermoelectric applications.



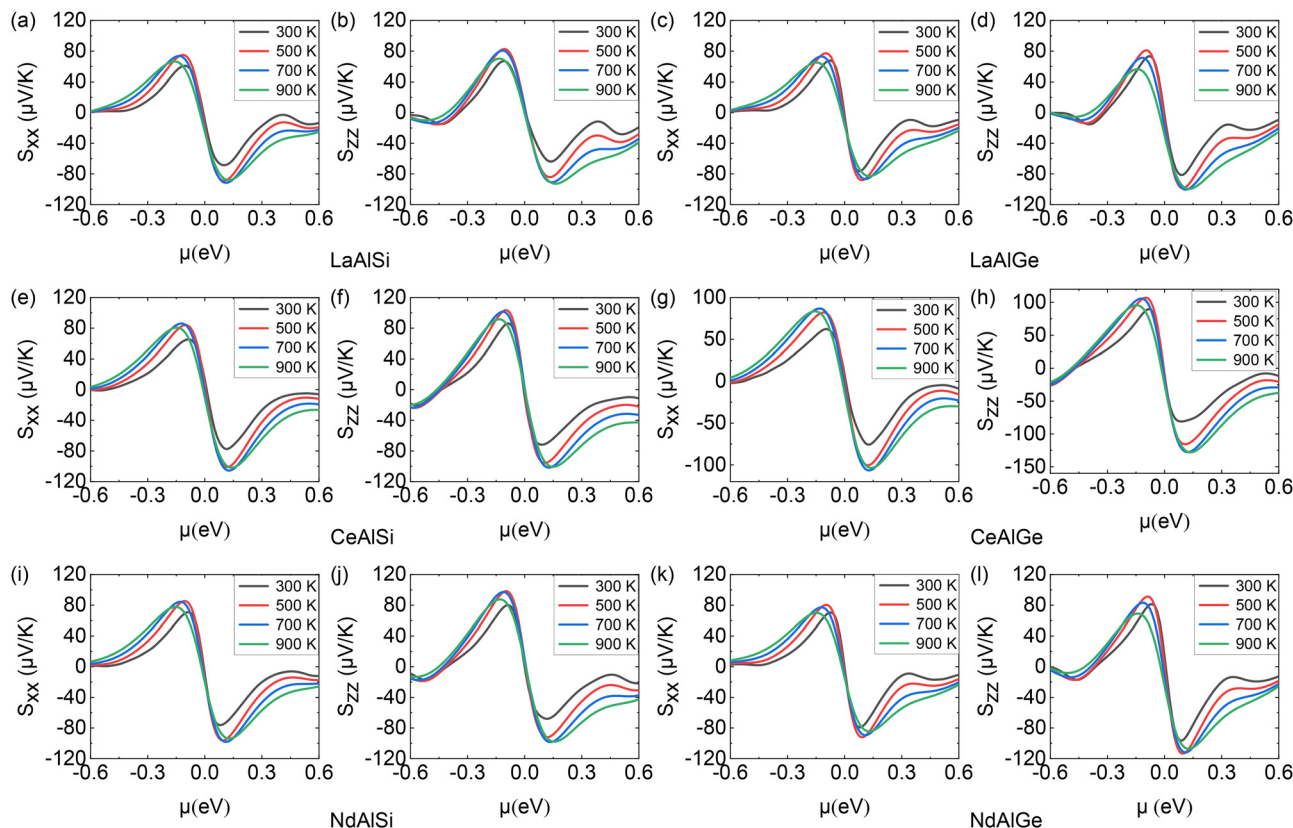


Fig. 5 Seebeck coefficients S as a function of chemical potential (set to 0 in the undoped state) shown at $T = 300$ K, 500 K, 700 K, and 900 K for each material along both the xx and zz directions. The n -doping shows higher values for maximum S than the p -doping. The peaked nature is due to the sensitive dependence of DOS on energy as seen in Fig. 2, which contributes to S due to the Mott relation (eqn (2)).

relaxation of the lattice constants and the atomic positions until the total force on individual atoms was less than $0.001 \text{ eV } \text{\AA}^{-1}$. The relaxed lattice constants are shown in Table 1 along with the experimental lattice constants.^{45,72–74} The relaxed Wyckoff positions are reported in Table S1 of our SI. Our optimized lattice constants are in good agreement with the experimentally reported values. To perform the DFT calculations we have used a primitive unit cell, which is shown in Fig. 1b.

3.2 Electronic band structure

The calculated band structures including Hubbard and SOC interactions for RAIX for $R = \text{Ce, La, Nd}$ and $X = \text{Si, Ge}$ are shown in Fig. 2. The linearly crossing bands can be seen along $\Sigma\text{--N--}\Sigma_1$, indicating the Weyl semimetal nature for all of them. The lack of inversion symmetry is the key player in this family, leading to Weyl fermions.²⁶ It has been shown that the magnetic nature of elements like Ce does not alter the magnetic band structure radically, and it can be treated as a Zeeman coupling, which splits the spin-up and spin-down bands.²⁶ This shifts the Weyl nodes in the Brillouin zone but can be reliably captured using first-principles calculations.²⁶ Due to the additional element in the choice of R , which can be magnetic, in the already broken inversion-symmetry phase of RAIX, this family of materials offers a rich phase diagram of phenomenology.²⁶ The calculated band structures presented here show excellent agreement with ARPES

results wherever available.^{27,28} The magnetic nature of $R = \text{Ce}$ and Nd plays an important role as the Weyl nodes are shifted, as compared to non-magnetic $R = \text{La}$, for these elements, while for non-magnetic $R = \text{La}$, the Weyl nodes occur closer to $E = E_F$. This plays a role in determining the thermoelectric properties, as the

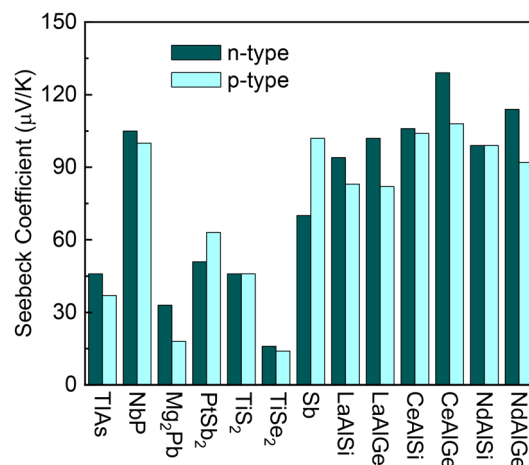


Fig. 6 Comparison of the Seebeck coefficient values for various topological materials (TlAs ,⁷⁵ NbP ,⁷⁵ Mg_2Pb ,⁷⁵ PtSb_2 ,⁷⁵ TiS_2 ,⁷⁵ TiSe_2 ,⁷⁵ Sb) with the RAIX family members in this study. The Seebeck coefficient values of the RAIX family are comparatively quite favorable.



location of Weyl nodes at the center may allow carriers of both polarities, leading to the cancellation of each other's contribution. Therefore, R = La shows the minimum values of the thermoelectric figure of merit zT in our results [Table 2].

The density of states (DOS) is plotted for all the materials adjacent to the band structure. DOS shows the characteristic semimetal nature with the minima at the Fermi level. The sharp dependence of DOS on energy close to the Fermi level enhances the Seebeck coefficient due to the Mott relation⁹ [Section 3.4 discusses this in detail]. The d-electrons of the R atom are the most significant contributors close to the Fermi-level, followed by the p-orbitals of the Al and X. The contribution of f-electrons is lower than these 3 orbitals near the Fermi-level in our calculations. R = La has no f electrons; therefore, its contribution appears in the conduction band and not in the valence band. f electrons can be seen in the valence band for R = Ce. These observations indicate that for electronic transport, which mostly consists of electrons close to the Fermi level, the d-electrons of the R atoms may play a major role, followed by p-orbitals of the Al and X atoms.

3.3 Phonon band structure and lattice thermal conductivity

The lattice plays a crucial role in the comprehensive understanding of thermal properties. Therefore, it is important to study the phonon dispersion relations, phonon DOS, and lattice thermal conductivity to evaluate a material's prospects as a viable thermoelectric. The phonon band structures for all the materials in this

study are shown in Fig. 3. There are 18 total modes ($3N$, for $N = 6$ atoms in our chosen unit cell), and the first 3 low-frequency modes are the acoustic modes, and the remaining 15 are the optical modes. The X = Ge members of the family have a much larger gap compared to the X = Si in the 6–9 THz frequency region because of the larger mismatch in the atomic masses of Al and Ge as compared to the X = Si where the atomic mass mismatch between Al and Si is much smaller. The phonon DOS is also plotted along each phonon dispersion. The 10–12 THz higher frequency phonon region is dominated by the lighter atom Al, and the heavier R atom dominates the low-frequency region near 4 THz. Multiple phonon modes display weak, almost flat dispersion and hybridization with the low-lying longitudinal acoustic modes. These regions correspond to the peaks in the phonon DOS, as multiple bands exist in a small energy region. This indicates low phonon velocity and significant phonon scattering channels leading to low thermal conductivity. This is a key factor for improved thermoelectric performance as seen from (1). Indeed, our calculations for thermal conductivities, as shown in Fig. 4, indicate that the thermal conductivities in both the xx and zz directions are approximately an order of magnitude smaller compared to the electronic thermal conductivities, which will be discussed in the next section. We note that the X = Si members have relatively higher thermal conductivities compared to the X = Ge by a factor of 2. This is due to the smaller phonon bandgap in X = Si compared to X = Ge, making it easier to excite

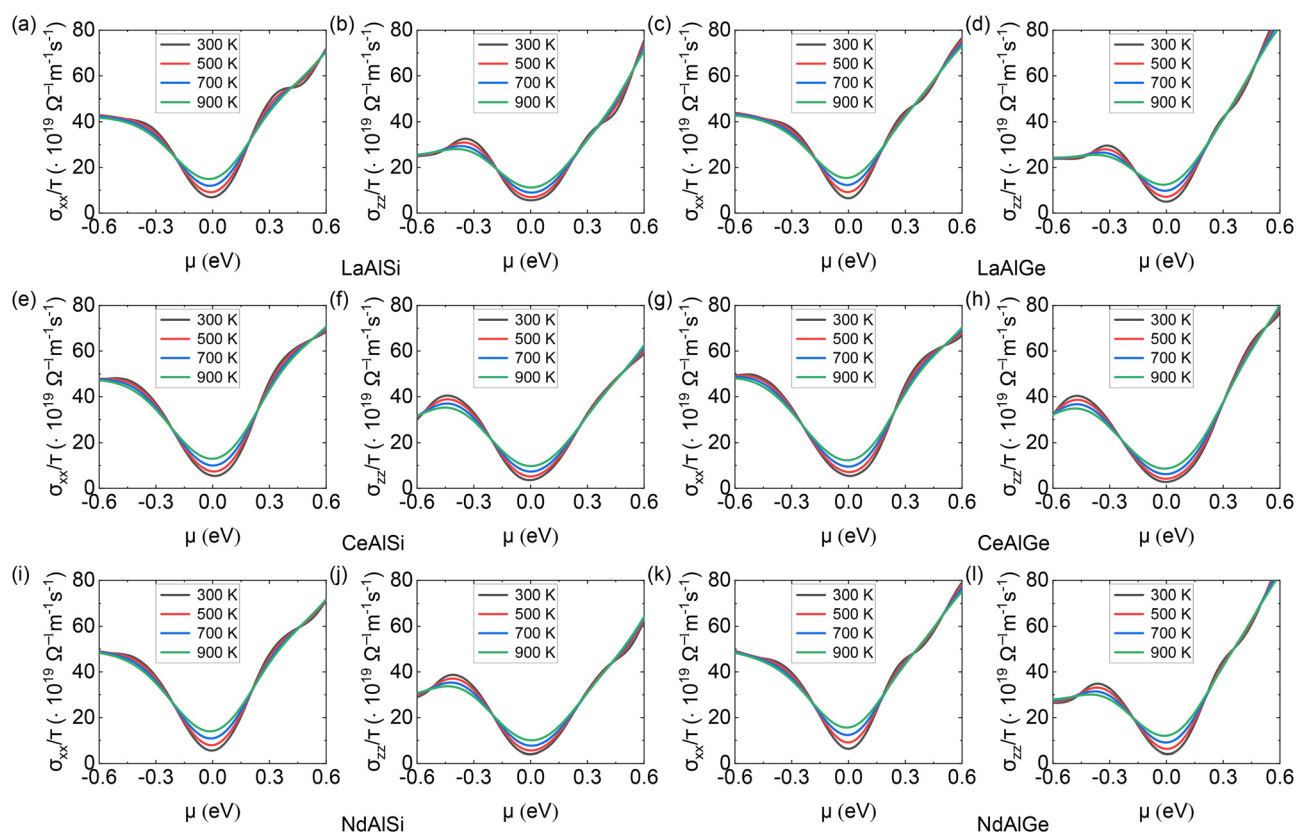


Fig. 7 Electrical conductivities σ/τ , within the constant relaxation time approximation of $\tau = 10^{-14}$ s [as discussed in Section 2], as a function of chemical potential (set to 0 in the undoped state) shown at $T = 300$ K, 500 K, 700 K, and 900 K for each material along both the xx and zz directions.



phonon modes contributing to lattice thermal conductivity. The low lattice thermal conductivities reported in our work may guide future research on this family of materials by ruling out much difference in thermoelectric performance by nanostructuring to reduce the phonon mean free path. These results also indicate that other phonon engineering methods may also not be very practical, as the electronic thermal conductivity will be the determining factor for the thermoelectric figure of merit.

3.4 Thermoelectric transport and key parameters

For semimetals, among the transport parameters determining the thermoelectric figure of merit, the sensitivity of S on scattering rate is minimal.⁷⁵ Moreover, zT depends on S quadratically. Therefore, S becomes the major player in the determination of the thermoelectric performance for semimetals. We show our calculated S values in Fig. 5 for all members of the family included in our studies. S_{ij} are calculated along both the xx and zz directions to look for anisotropy. The results show moderate anisotropy, with CeAlGe showing the most and LaAlX showing the minimum anisotropy. The maximum value of $129 \mu\text{V K}^{-1}$ is obtained for n-type doping in CeAlGe at 900 K. The peaked nature in S has been seen in other Weyl semimetals such as TaAs⁵⁴ and can be attributed to the sensitive dependence of the DOS on the energy $\partial N/\partial \varepsilon$ as shown in the DOS plots in Fig. 2, which contribute

to the S as per the Mott relation.⁹

$$S = \frac{\pi^2 k_B^2 T}{3e} \left[\frac{1}{n} \frac{\partial n(\varepsilon)}{\partial \varepsilon} + \frac{1}{\mu} \frac{\partial \mu(\varepsilon)}{\partial \varepsilon} \right]_{\varepsilon=\mu} \quad (2)$$

We compare the maximum S of other semimetals⁷⁵ with our calculations of RAlX in Fig. 6 for both n-type and p-type. The RAlX family shows quite significant values of S compared to other semimetals.

Electrical conductivity σ_{ij}/τ is calculated along xx and zz as shown in Fig. 7. All compounds in this study show a fair bit of anisotropy for electrical conductivity. The shape of the conductivity curve is typical for semimetallic nature⁵⁴ as expected in this family with a minimum close to $E = E_F$. The trend in conductivity roughly follows the density of states as it is the central factor determining the conductivity and therefore we get an approximately V shaped curve for semimetals as their conduction and valence bands merely touch at the Fermi level leading to low density of states at the Fermi level, but higher density of states in the conduction and valence bands.

Calculated electronic thermal conductivities are presented in Fig. 8. Due to the Wiedemann–Franz law, the electronic thermal conductivity is proportional to the electrical conductivity.¹² Thus, the κ^{el} roughly follows the same trend as the electrical conductivity and underlines the difficulty of

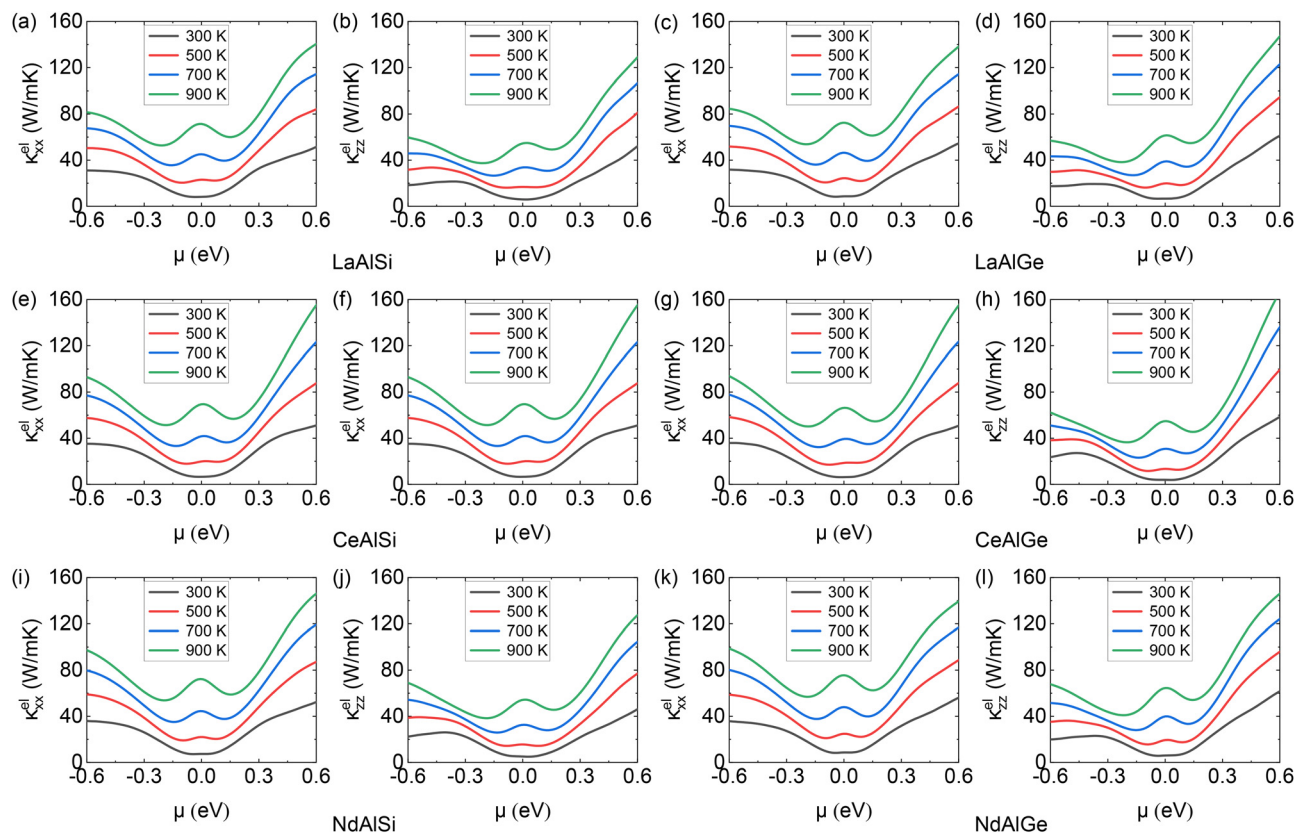


Fig. 8 Electronic thermal conductivities κ , within the constant relaxation time approximation of $\tau = 10^{-14}$ s [as discussed in Section 2] as a function of chemical potential (set to 0 in the undoped state) shown at $T = 300$ K, 500 K, 700 K, and 900 K for each material along both the xx and zz directions. The temperature-dependent small peak near 0 chemical potential may be attributed to thermally excited carriers.



optimizing the power factor. Close to the Fermi level, we can see a difference in behavior as there is a small temperature-dependent peak. This may occur due to the polarity compensation of charge carriers at elevated temperatures. This leads to a dip at finite doping and may be favorable for thermoelectric performance as this is approximately also the region where the Seebeck coefficient S peaks. The electronic thermal conductivities are an order of magnitude higher than the lattice thermal conductivities, which makes them the dominant player in the thermoelectric figure of merit. Therefore, our studies suggest that the optimization techniques for the thermoelectric materials should focus on band engineering and optimization to improve electronic parameters, as the lattice thermal conductivity is an order of magnitude lower than the electronic thermal conductivity. Nanostructuring and other lattice thermal conductivity optimization techniques may not yield much improvement.

In all these electronic transport parameters: the Seebeck coefficient S , electrical conductivity σ , and thermal conductivity κ , we notice a common trend of higher values for $\mu > 0$ leading to an anisotropy with respect to μ . This can be attributed to the greater number of bands contributing to the transport above the Fermi level rather than below the Fermi level as can be seen in the band structures between the Σ and Z points in Fig. 2. Another

common feature in all the reported electronic transport parameters is that the anisotropy in the parameters in μ is more pronounced for the transport parameters along the zz direction as compared to the xx direction. This implies that the band density in the Brillouin zone (BZ) corresponding to the zz direction for the conduction band is higher in this tetragonal family of compounds. This information as indicated in our results may help choose the material orientation in future devices.

After studying each ingredient going into the thermoelectric figure of merit (1), we show our calculated thermoelectric figure of merit in Fig. 9 for both the xx and zz directions. Based on the values of S , σ and κ , where κ^{el} is dominating over κ^{l} as per our calculations, we observe the peaks at the locations where S is maximum and κ^{el} is minimum. CeAlGe shows the maximum values among all members in our results with $zT = 0.56$ at a chemical potential $\mu = 0.19$ at $T = 900$ K. The maximum zT for all RAlX occurs for n-type doping. LaAlSi, LaAlGe, CeAlSi, and NdAlGe show higher zT along zz . CeAlSi shows a higher zT along xx . NdAlSi shows the same value of zT for both xx and zz . The maximum values of zT for all materials and their corresponding μ and temperature values are reported in Table 2. R = Ce and Nd show higher values than R = La, for a given X atom. This is because the electronic band structure of La shows that the Weyl nodes are closer to the Fermi level, compared to others, which may lead to

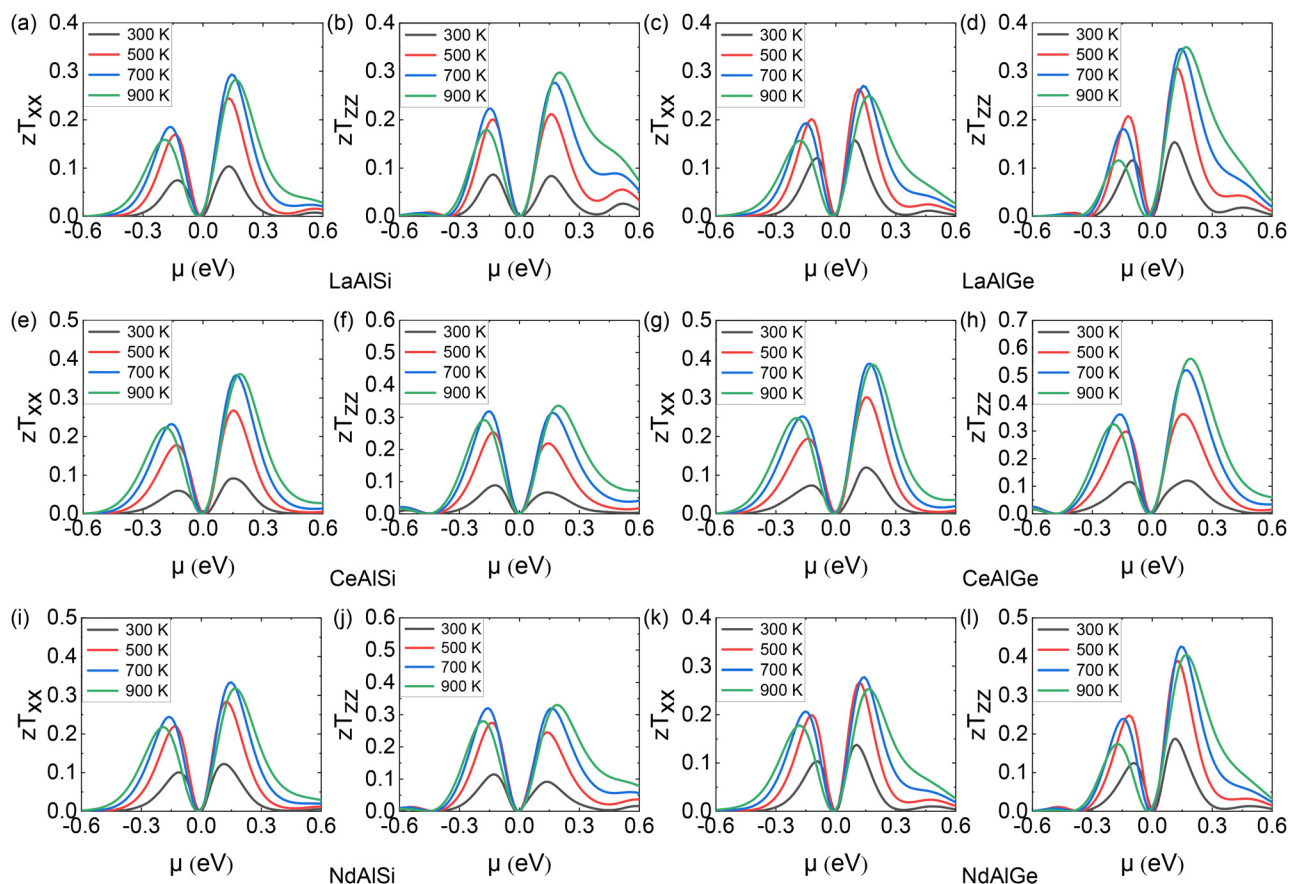


Fig. 9 Figure of merit zT , within the constant relaxation time approximation of $\tau = 10^{-14}$ s [as discussed in Section 2] as a function of chemical potential (set to 0 in the undoped state) shown at $T = 300$ K, 500 K, 700 K, and 900 K for each material along both the xx and zz directions.



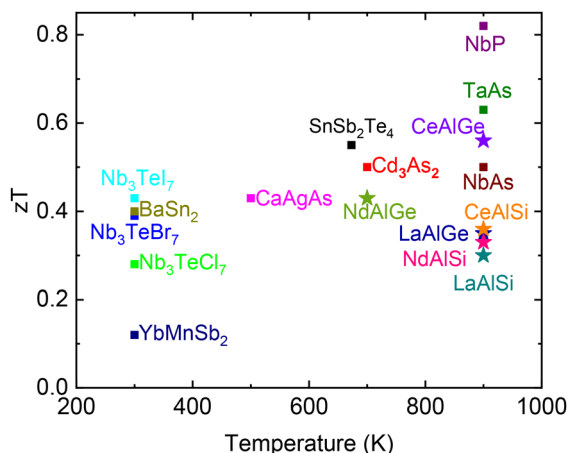


Fig. 10 Comparison of maximum zT values for various topological materials (YbMnSb₂,⁷⁶ Nb₃TeI₇,⁷⁷ Nb₃TeBr₇,⁷⁷ Nb₃TeCl₇,⁷⁷ BaSn₂,⁷⁸ CaAgAs,⁷⁹ Cd₃As₂,⁸⁰ SnSb₂Te₄,⁸¹ NbAs,⁵⁸ TaAs,⁸² NbP²⁴) with the RAlX family members in this study. Our results show encouraging numbers for the RAlX family (denoted by star symbols).

compensation of the carriers and thus a low value of S . Indeed, our calculations show that the maximum value S for LaAlX is the lowest among all the RAlX we have considered in this study. Among Ce and Nd, Ce shows a higher value of S , and since zT depends on S quadratically, zT for CeAlX is higher than that of NdAlX.

Fig. 10 shows the thermoelectric figure of merit calculated in our studies for RAlX compared with other topological materials^{58,76–82} to place our results in context. In terms of topological semimetals, the thermoelectric figures of merit revealed in our studies are quite encouraging.

4. Conclusions

In conclusion, we have performed a detailed first-principles study of thermoelectric properties of an important class of materials RAlX for R = La, Ce, Nd and X = Si, Ge using both phonon and electron transport, including Hubbard and spin-orbit interactions. We have shown that they possess low lattice thermal conductivity by an order of magnitude compared to electronic thermal conductivity. This makes them good candidates for potential thermoelectric use by performing electronic band engineering and doping. Our results show moderate anisotropy in transport in the xx and zz directions. We have calculated the thermoelectric figure of merit zT for all members and found the highest value of 0.56 for CeAlGe at 900 K with electron doping. R = Ce and R = Nd both seem to have higher values than R = La. A close look at the electronic band structure reveals that the Weyl nodes are not exactly at the Fermi level for R = Ce and R = Nd, but they are closer to the Fermi level for R = La. This is possibly due to magnetization in the R = Ce and R = Nd bands, which acts as a Zeeman shift.²⁶ This leads to an imbalance in the carrier compensation, which would lead to better thermoelectric performance as compared to the compensated semimetal for R = La, where magnetization plays no role. CeAlX possesses a higher value than NdAlX as our

first-principles calculations reveal that it has a higher value of S . Even though the zT numbers may not compare with traditional semiconducting/small-gap thermoelectrics, these materials show multiple interesting phenomena, including type-II Lorentz-violating Weyl fermions, ultrahigh mobility, and chiral behavior, among others. Therefore, our studies reveal that RAlX have the potential to be an interesting playground for multiple quantum phenomena making them excellent candidates for multifunctional quantum materials. Overall, our study has shed light on the thermoelectric properties of this exciting family of materials and will assist in future investigations and experiments.

Author contributions

R. S. and S. C. conceived the project. S. C. performed the calculations aided by P. T. and K. A. P. R. S. and S. C. wrote the manuscript with contributions from all authors.

Conflicts of interest

There are no conflicts to declare.

Data availability

All the data and methods underlying this manuscript are presented in the paper. The authors can be contacted for any further clarification.

Supplementary information (SI) is available. See DOI: <https://doi.org/10.1039/d5tc02363g>.

Acknowledgements

This work has been performed with research supported by the Startup-Research Grant (SRG) of the, Science and Engineering Research Board (SERB), Department of Science and Technology (DST), Government of India, with reference to file no. SRG/2023/001274. We acknowledge the research support from the High-Performance Computing facility at the Central Advanced Instrument Facility (CAIF) at the Indian Institute of Science Education and Research (IISER) Berhampur.

References

- 1 L. E. Bell, *Science*, 2008, **321**, 1457–1461.
- 2 G. Tan, L.-D. Zhao and M. G. Kanatzidis, *Chem. Rev.*, 2016, **116**, 12123–12149.
- 3 T. Zhu, Y. Liu, C. Fu, J. P. Heremans, J. G. Snyder and X. Zhao, *Adv. Mater.*, 2017, **29**, 1605884.
- 4 P. Baskaran and M. Rajasekar, *RSC Adv.*, 2024, **14**, 21706–21744.
- 5 X.-L. Shi, W.-Y. Chen, T. Zhang, J. Zou and Z.-G. Chen, *Energy Environ. Sci.*, 2021, **14**, 729–764.
- 6 X.-L. Shi, L. Wang, W. Lyu, T. Cao, W. Chen, B. Hu and Z.-G. Chen, *Chem. Soc. Rev.*, 2024, **53**, 9254–9305.



- 7 M. Zeng, D. Zavanelli, J. Chen, M. Saeidi-Javash, Y. Du, S. LeBlanc, G. J. Snyder and Y. Zhang, *Chem. Soc. Rev.*, 2022, **51**, 485–512.
- 8 Y. Pei, X. Shi, A. LaLonde, H. Wang, L. Chen and G. J. Snyder, *Nature*, 2011, **473**, 66–69.
- 9 J. Yang, L. Xi, W. Qiu, L. Wu, X. Shi, L. Chen, J. Yang, W. Zhang, C. Uher and D. J. Singh, *npj Comput. Mater.*, 2016, **2**, 15015.
- 10 H. Han, L. Zhao, X. Wu, B. Zuo, S. Bian, T. Li, X. Liu, Y. Jiang, C. Chen, J. Bi, J. Xu and L. Yu, *J. Mater. Chem. A*, 2024, **12**, 24041–24083.
- 11 M. Mukherjee, A. Srivastava and A. K. Singh, *J. Mater. Chem. C*, 2022, **10**, 12524–12555.
- 12 N. W. Ashcroft and N. D. Mermin, *Solid state physics*, Cengage Learning, New Delhi, 1976.
- 13 K. Pal, S. Anand and U. V. Waghmare, *J. Mater. Chem. C*, 2015, **3**, 12130–12139.
- 14 A. A. Zyuzin and A. A. Burkov, *Phys. Rev. B: Condens. Matter Mater. Phys.*, 2012, **86**, 115133.
- 15 J. Xiong, S. K. Kushwaha, T. Liang, J. W. Krizan, M. Hirschberger, W. Wang, R. J. Cava and N. P. Ong, *Science*, 2015, **350**, 413–416.
- 16 A. A. Burkov, *J. Phys.: Condens. Matter*, 2015, **27**, 113201.
- 17 N. P. Ong and S. Liang, *Nat. Rev. Phys.*, 2021, **3**, 394–404.
- 18 A. Lucas, R. A. Davison and S. Sachdev, *Proc. Natl. Acad. Sci. U. S. A.*, 2016, **113**, 9463–9468.
- 19 V. Kozii, B. Skinner and L. Fu, *Phys. Rev. B*, 2019, **99**, 155123.
- 20 F. Han, N. Andrejevic, T. Nguyen, V. Kozii, Q. T. Nguyen, T. Hogan, Z. Ding, R. Pablo-Pedro, S. Parjan, B. Skinner, A. Alatas, E. Alp, S. Chi, J. Fernandez-Baca, S. Huang, L. Fu and M. Li, *Nat. Commun.*, 2020, **11**, 6167.
- 21 J. Corps, P. Vaqueiro, A. Aziz, R. Grau-Crespo, W. Kockelmann, J.-C. Jumas and A. V. Powell, *Chem. Mater.*, 2015, **27**, 3946–3956.
- 22 H. Wang, Z. Zhou, J. Ying, Z. Xiang, R. Wang, A. Wang, Y. Chai, M. He, X. Lu, G. Han, Y. Pan, G. Wang, X. Zhou and X. Chen, *Adv. Mater.*, 2023, **35**, 2206941.
- 23 Y. Pan, B. He, T. Helm, D. Chen, W. Schnelle and C. Felser, *Nat. Commun.*, 2022, **13**, 3909.
- 24 Y. Zhou, Y.-Q. Zhao, Z.-Y. Zeng, X.-R. Chen and H.-Y. Geng, *Phys. Chem. Chem. Phys.*, 2019, **21**, 15167–15176.
- 25 C. Shekhar, A. K. Nayak, Y. Sun, M. Schmidt, M. Nicklas, I. Leermakers, U. Zeitler, Y. Skourski, J. Wosnitza, Z. Liu, Y. Chen, W. Schnelle, H. Borrmann, Y. Grin, C. Felser and B. Yan, *Nat. Phys.*, 2015, **11**, 645–649.
- 26 G. Chang, B. Singh, S.-Y. Xu, G. Bian, S.-M. Huang, C.-H. Hsu, I. Belopolski, N. Alidoust, D. S. Sanchez, H. Zheng, H. Lu, X. Zhang, Y. Bian, T.-R. Chang, H.-T. Jeng, A. Bansil, H. Hsu, S. Jia, T. Neupert, H. Lin and M. Z. Hasan, *Phys. Rev. B*, 2018, **97**, 041104.
- 27 A. P. Sakhyia, C.-Y. Huang, G. Dhakal, X.-J. Gao, S. Regmi, B. Wang, W. Wen, R.-H. He, X. Yao, R. Smith, M. Sprague, S. Gao, B. Singh, H. Lin, S.-Y. Xu, F. Tafti, A. Bansil and M. Neupane, *Phys. Rev. Mater.*, 2023, **7**, L051202.
- 28 S.-Y. Xu, N. Alidoust, G. Chang, H. Lu, B. Singh, I. Belopolski, D. S. Sanchez, X. Zhang, G. Bian, H. Zheng, M.-A. Husanu, Y. Bian, S.-M. Huang, C.-H. Hsu, T.-R. Chang, H.-T. Jeng, A. Bansil, T. Neupert, V. N. Strocov, H. Lin, S. Jia and M. Z. Hasan, *Sci. Adv.*, 2017, **3**, e1603266.
- 29 A. A. Soluyanov, D. Gresch, Z. Wang, Q. Wu, M. Troyer, X. Dai and B. A. Bernevig, *Nature*, 2015, **527**, 495–498.
- 30 T. M. McCormick, R. C. McKay and N. Trivedi, *Phys. Rev. B*, 2017, **96**, 235116.
- 31 B. Jiang, L. Wang, R. Bi, J. Fan, J. Zhao, D. Yu, Z. Li and X. Wu, *Phys. Rev. Lett.*, 2021, **126**, 236601.
- 32 P. Puphal, V. Pomjakushin, N. Kanazawa, V. Ukleev, D. J. Gawryluk, J. Ma, M. Naamneh, N. C. Plumb, L. Keller, R. Cubitt, E. Pomjakushina and J. S. White, *Phys. Rev. Lett.*, 2020, **124**, 017202.
- 33 H. Hodovanets, C. J. Eckberg, D. J. Campbell, Y. Eo, P. Y. Zavalij, P. Piccoli, T. Metz, H. Kim, J. S. Higgins and J. Paglione, *Phys. Rev. B*, 2022, **106**, 235102.
- 34 N. C. Drucker, T. Nguyen, F. Han, P. Siriviboon, X. Luo, N. Andrejevic, Z. Zhu, G. Bednik, Q. T. Nguyen, Z. Chen, L. K. Nguyen, T. Liu, T. J. Williams, M. B. Stone, A. I. Kolesnikov, S. Chi, J. Fernandez-Baca, C. S. Nelson, A. Alatas, T. Hogan, A. A. Puzetzy, S. Huang, Y. Yu and M. Li, *Nat. Commun.*, 2023, **14**, 5182.
- 35 M. M. Piva, J. C. Souza, G. A. Lombardi, K. R. Pakuszewski, C. Adriano, P. G. Pagliuso and M. Nicklas, *Phys. Rev. Mater.*, 2023, **7**, 074204.
- 36 H. Su, X. Shi, J. Yuan, Y. Wan, E. Cheng, C. Xi, L. Pi, X. Wang, Z. Zou, N. Yu, W. Zhao, S. Li and Y. Guo, *Phys. Rev. B*, 2021, **103**, 165128.
- 37 J. Kunze, M. Köpf, W. Cao, Y. Qi and C. A. Kuntscher, *Phys. Rev. B*, 2024, **109**, 195130.
- 38 W. Kohn and L. J. Sham, *Phys. Rev.*, 1965, **140**, A1133–A1138.
- 39 P. Hohenberg and W. Kohn, *Phys. Rev.*, 1964, **136**, B864–B871.
- 40 P. E. Blöchl, *Phys. Rev. B: Condens. Matter Mater. Phys.*, 1994, **50**, 17953–17979.
- 41 P. Giannozzi, *et al.*, *J. Phys.: Condens. Matter*, 2009, **21**, 395502.
- 42 P. Giannozzi, *et al.*, *J. Phys.: Condens. Matter*, 2017, **29**, 465901.
- 43 J. P. Perdew, K. Burke and M. Ernzerhof, *Phys. Rev. Lett.*, 1996, **77**, 3865–3868.
- 44 H. J. Monkhorst and J. D. Pack, *Phys. Rev. B: Condens. Matter Mater. Phys.*, 1976, **13**, 5188–5192.
- 45 C. Dhital, R. L. Dally, R. Ruvalcaba, R. Gonzalez-Hernandez, J. Guerrero-Sanchez, H. B. Cao, Q. Zhang, W. Tian, Y. Wu and M. D. Frontzek, *et al.*, *Phys. Rev. B*, 2023, **107**, 224414.
- 46 A. P. Sakhyia, C.-Y. Huang, G. Dhakal, X.-J. Gao, S. Regmi, B. Wang, W. Wen, R.-H. He, X. Yao and R. Smith, *et al.*, *Phys. Rev. Mater.*, 2023, **7**, L051202.
- 47 H.-Y. Yang, B. Singh, J. Gaudet, B. Lu, C.-Y. Huang, W.-C. Chiu, S.-M. Huang, B. Wang, F. Bahrami and B. Xu, *et al.*, *Phys. Rev. B*, 2021, **103**, 115143.
- 48 C. Li, J. Zhang, Y. Wang, H. Liu, Q. Guo, E. Rienks, W. Chen, F. Bertran, H. Yang and D. Phuyal, *et al.*, *Nat. Commun.*, 2023, **14**, 7185.
- 49 J. Gaudet, H.-Y. Yang, S. Baidya, B. Lu, G. Xu, Y. Zhao, J. A. Rodriguez-Rivera, C. M. Hoffmann, D. E. Graf and D. H. Torchinsky, *et al.*, *Nat. Mater.*, 2021, **20**, 1650–1656.



- 50 P. Hosur, S. A. Parameswaran and A. Vishwanath, *Phys. Rev. Lett.*, 2012, **108**, 046602.
- 51 R. Lundgren, P. Laurell and G. A. Fiete, *Phys. Rev. B: Condens. Matter Mater. Phys.*, 2014, **90**, 165115.
- 52 G. K. Madsen and D. J. Singh, *Comput. Phys. Commun.*, 2006, **175**, 67–71.
- 53 G. K. Madsen, J. Carrete and M. J. Verstraete, *Comput. Phys. Commun.*, 2018, **231**, 140–145.
- 54 B. Peng, H. Zhang, H. Shao, H. Lu, D. W. Zhang and H. Zhu, *Nano Energy*, 2016, **30**, 225–234.
- 55 A. Shukla, S. Matth, R. Pal, S. S. A. Warsi and H. Pandey, *AIP Adv.*, 2025, **15**, 015208.
- 56 S. Ramawat, S. Kukreti and A. Dixit, *Phys. Rev. Mater.*, 2023, **7**, 085403.
- 57 K. Pal, S. Anand and U. V. Waghmare, *J. Mater. Chem. C*, 2015, **3**, 12130–12139.
- 58 Y. Zhou, Y.-Q. Zhao, Z.-Y. Zeng, X.-R. Chen and H.-Y. Geng, *Phys. Chem. Chem. Phys.*, 2019, **21**, 15167–15176.
- 59 S. Bouhmaidi, A. Marjaoui, A. Talbi, M. Zanouni, K. Nouneh and L. Setti, *Comput. Condens. Matter*, 2022, **31**, e00663.
- 60 J. L. Ponce-Ruiz, S. Ishizuka, Y. Todaka, Y. Yamada, A. R. Serrato and J. Herrera-Ramirez, *ACS Omega*, 2022, **7**, 15451–15458.
- 61 S. Nath, *J. Appl. Phys.*, 2021, **130**, 055106.
- 62 R. Viennois, M. M. Koza, A. Moll and M. Beaudhuin, *Phys. Chem. Chem. Phys.*, 2023, **25**, 1987–1997.
- 63 A. Azam, R. Sharma, D. Behera, H. H. Raza, H. S. Ali, S. A. Abdelmohsen, A. M. Abdelbacki and S. K. Mukherjee, *RSC Adv.*, 2023, **13**, 15437–15447.
- 64 R. Farris, M. B. Maccioni, A. Filippetti and V. Fiorentini, *J. Phys.: Condens. Matter*, 2018, **31**, 065702.
- 65 J.-H. Pöhls, A. Faghaninia, G. Petretto, U. Aydemir, F. Ricci, G. Li, M. Wood, S. Ohno, G. Hautier and G. J. Snyder, *et al.*, *J. Mater. Chem. C*, 2017, **5**, 12441–12456.
- 66 A. Togo, L. Chaput, T. Tadano and I. Tanaka, *J. Phys.: Condens. Matter*, 2023, **35**, 353001.
- 67 A. Togo, *J. Phys. Soc. Jpn.*, 2023, **92**, 012001.
- 68 S. Baroni, S. de Gironcoli, A. Dal Corso and P. Giannozzi, *Rev. Mod. Phys.*, 2001, **73**, 515.
- 69 F. Giustino, M. L. Cohen and S. G. Louie, *Phys. Rev. B: Condens. Matter Mater. Phys.*, 2007, **76**, 165108.
- 70 A. A. Mostofi, J. R. Yates, Y.-S. Lee, I. Souza, D. Vanderbilt and N. Marzari, *Comput. Phys. Commun.*, 2008, **178**, 685–699.
- 71 Q. Wu, S. Zhang, H.-F. Song, M. Troyer and A. A. Soluyanov, *Comput. Phys. Commun.*, 2018, **224**, 405–416.
- 72 W. Cao, N. Zhao, C. Pei, Q. Wang, Q. Zhang, T. Ying, Y. Zhao, L. Gao, C. Li and N. Yu, *et al.*, *Phys. Rev. B*, 2022, **105**, 174502.
- 73 T. Wang, Y. Guo and C. Wang, *Chin. Phys. B*, 2021, **30**, 075102.
- 74 H. Hodovanets, C. Eckberg, P. Zavalij, H. Kim, W.-C. Lin, M. Zic, D. Campbell, J. Higgins and J. Paglione, *Phys. Rev. B*, 2018, **98**, 245132.
- 75 M. Markov, S. E. Rezaei, S. N. Sadeghi, K. Esfarjani and M. Zebarjadi, *Phys. Rev. Mater.*, 2019, **3**, 095401.
- 76 Y. Pan, F.-R. Fan, X. Hong, B. He, C. Le, W. Schnelle, Y. He, K. Imasato, H. Borrmann and C. Hess, *et al.*, *Adv. Mater.*, 2021, **33**, 2003168.
- 77 W.-Y. Fang, X.-X. Rao, K. Jin, S.-A. Chen, X.-F. Sheng and L. Bao, *Vacuum*, 2024, **219**, 112725.
- 78 S.-D. Guo and L. Qiu, *J. Phys. D: Appl. Phys.*, 2016, **50**, 015101.
- 79 N. Kumar, N. Sheoran and H. S. Saini, *Phys. Status Solidi B*, 2024, **261**, 2400187.
- 80 T. Zhou, C. Zhang, H. Zhang, F. Xiu and Z. Yang, *Inorg. Chem. Front.*, 2016, **3**, 1637–1643.
- 81 S. Das, D. Sarkar and K. Biswas, *Chem. Mater.*, 2024, **36**, 3359–3368.
- 82 B. Peng, H. Zhang, H. Shao, H. Lu, D. W. Zhang and H. Zhu, *Nano Energy*, 2016, **30**, 225–234.

